A study of dissipation of wind-waves by mud at Cassino Beach, Brazil: Prediction and inversion

W. Erick Rogers [a,*], K. Todd Holland [b]

[a] Naval Research Laboratory (NRL) Oceanography Division; Code 7322; Stennis Space Center, MS 39529, USA
[b] NRL Marine Geosciences Division; Code 7440.3; Stennis Space Center, MS 39529, USA

ARTICLE INFO

ABSTRACT

The impact of a non-rigid seafloor on the wave climate at Cassino Beach, Brazil, May–June 2005 is studied using field measurements and a numerical wave model. The measurements consist of wave data at four locations; rheology and mud thickness from grab samples; and an estimate of the horizontal distribution of mud based on echo-soundings. The dissipation of waves by a non-rigid bottom is represented in the wave model by treating the mud layer as a viscous fluid. Applied for 431 time periods, the model without this type of dissipation has a strong tendency to overpredict nearshore wave energy, except during a period of large storm waves. Two model variations which include this dissipation have a modest tendency to underpredict the nearshore wave energy. An inversion methodology is developed and applied to infer an alternate mud distribution which, when used with the wave model, yields the observed waveheights.

Published by Elsevier Ltd.

1. Introduction

Wind-generated surface waves in shallow and intermediate depths generate pressure variations at the seabed with spatial and temporal scales corresponding to the wavelength and wave period. In the case of a non-rigid bottom, such as mud, the pressure variations can result in motion of the water/seabed interface. Work is being done to generate this motion, and thus energy is lost from the wind-waves. In the case of a muddy bottom, the motion in the seabed is subsequently damped, predominately by viscosity.

Methods exist for estimating the damping of water waves by viscous mud. An early effort was made by Gade (1958), using an assumption of shallow water. Dalrymple and Liu (1978) developed a more general method without using this assumption; further, their method accounts for viscosity in the water, rather than just

the mud layer. Ng (2000) proposed a numerical simplification of the Dalrymple and Liu (1978) calculation, using an assumption of a thin mud layer. Such treatments of non-rigid seafloor as a viscous fluid do have limitations: mud can also exhibit viscoelastic or plastic behavior: see Hsiao and Shemdin (1980); Jiang and Mehta (1995, 1996); Zhang and Ng (2006); Mei and Liu (1987), and references therein.

Treatment of damping by wave-bottom interaction within an analytical wave model requires the a priori assumption that unrepresented processes (refraction, shoaling, wind effects, breaking, etc.) are small. For verification with field data, this assumption means that test cases must be very carefully selected, with most data sets being unsuitable. Treatment within a numerical wave model greatly improves this situation since these processes can be efficiently incorporated. One such model is the SWAN wave model, introduced in the 1990s (Holthuijsen et al., 1993; Ris 1997; Booij et al., 1999) for the purpose of predicting wave propagation, growth, and decay in coastal regions, and has since seen considerable use by scientists and engineers. However, this model includes parameterizations for attenuation via interaction with a *rigid* seafloor only. Even in early evaluations of the model, it was noted that the absence of mud-related dissipation is a major

* Corresponding author. Tel.: +1 228 688 4727; fax: +1 228 688 4759.
E-mail addresses: rogers@nrlssc.navy.mil (W. Erick Rogers),
tholland@nrlssc.navy.mil (K. Todd Holland).

Nomenclature

T_p	peak wave period
σ	wave angular frequency
$D(\theta)$	normalized directional distribution of wave energy
k	wavenumber
h	water layer thickness (without motion)
$\delta_{m,0}$	fluidized mud layer thickness (without motion)
$\delta_{m,0,t}$	total mud layer thickness (without motion)
ρ_w	water density
ρ_m	mud density
γ	ratio $\gamma = \rho_w/\rho_m$
v_w	kinematic viscosity of water layer
v_m	kinematic viscosity of mud layer
Δ_m	Stokes boundary layer thickness, $\Delta_m = \sqrt{v_m/\sigma}$
ζ	ratio $\zeta = \Delta_m/\Delta_w = (v_m/v_w)^{1/2}$
$\tilde{d}$	normalized mud layer depth (Reynolds number), $\tilde{d} = \delta_{m,0}/\Delta_m$
k_i	imaginary part of wavenumber, equivalent to the dissipation rate
$D_{m/w}$ or k_i	dissipation rate from viscosity in the mud and water layers, in the case of Ng and DL formulae, $D_{m/w} = k_i$
D_m	dissipation rate from viscosity in the mud layer, in the case of WDGL, $D_m = k_i$
D_w	dissipation rate from viscosity in the water layer
k_s	real part of the wave number in shallow water, $k_s = \sigma/\sqrt{gh}$
$x_{a=0.5a_0}$	distance over which a wave will be reduced to 50% of its original amplitude (see Eq. (1))
$x_{a=0.5a_0}$	distance over which a wave will be reduced to 10% of its original amplitude (see Eq. (1))
S_{ds}	spectral dissipation rate
S_{bot}	spectral dissipation rate from wave-bottom interaction, a subset of S_{ds}
S_{mud}	spectral dissipation rate from mud, a subset of S_{bot}
E	spectral energy density
N	spectral action density $N = E/\sigma$

deficiency, such that in cases of non-rigid seafloor, one must apply unrealistic bottom friction parameters to get the desired dissipation (e.g. Dingemans, 1998). Representation of damping by mud was recently introduced in SWAN by Winterwerp et al. (2007), based on an extension by De Wit (1995) of the Gade (1958) formulation, though at time of writing, it has not been incorporated into publicly released versions of the code (Holthuijsen et al., 2006). Winterwerp et al. (2007) utilize laboratory experiments with measured rheology by De Wit (1995). No prior numerical wave modeling study involves the application of field measurements of rheology; in Winterwerp et al. (2007), the field rheology is assumed.

The primary objective of the present study is to use numerical wave models to simulate wave dissipation by fluid mud, utilizing field measurements of both mud and wave conditions. The field experiment was held at Cassino Beach, Brazil during May–June 2005. Large numbers of simulations with the SWAN wave model over a 35-day period are performed to identify trends and sensitivity to physics of wave dissipation by viscous mud in this application. Secondary objectives are as follows: (i) to compare two methods for representing the dissipation of wind-generated surface waves by a viscous mud layer: the method of Winterwerp et al. (2007) and that of Ng (2000), the latter implemented in an experimental version of the SWAN model in this study; (ii) to determine whether including dissipation by mud is necessary for accurately reproducing observed wave heights; (iii) to, given an estimate of rheology and mud distribution derived from field measurements, evaluate the skill of these models in predicting observed wave heights; and (iv) to develop and apply an inversion process to determine the rheology and mud distribution for which the wave model will reproduce the observed wave heights.

Section 2 of this manuscript introduces the modeling platform, SWAN, as well as the two methods of representing dissipation by mud in this platform. The methods are also verified in this section, including a comparison with results using the approach of Dalrymple and Liu (1978). In Section 3, the Cassino Beach case study is introduced. In Section 4, the two-dimensional model design is described, and results are presented. In Section 5, the one-dimensional model design is described and results given. Also in this section, the inverse methodology is introduced, applied, and results given. Discussion is given in Section 6, and conclusions in Section 7.

2. Model description and verification

2.1. SWAN wave prediction model

The so-called "third generation" (3G) of spectral wave models calculate wave spectra without a priori assumptions regarding spectral shape. For this investigation, we use the SWAN model ("Simulating WAves Nearshore"; Booij et al., 1999; Holthuijsen et al., 2006). SWAN is a 3G model designed to address the excessive computational expense of applying predecessor 3G models (such as WAM, WAMDI Group, 1988) at high resolutions, particularly in coastal regions. The governing equation of SWAN and most other 3G wave models is the action balance equation. In Cartesian coordinates, the action balance equation is

$$\frac{\partial N}{\partial t} + \frac{\partial C_x N}{\partial x} + \frac{\partial C_y N}{\partial y} + \frac{\partial C_\sigma N}{\partial \sigma} + \frac{\partial C_\theta N}{\partial \theta} = \frac{S}{\sigma}$$

where σ is the angular relative frequency, which is the wave frequency measured from the frame of reference moving with current, if current exists, N is wave action density, equal to energy density divided by relative frequency ($N = E/\sigma$), θ is wave direction, C is the wave action propagation speed in (x, y, σ, θ) space, e.g. in absence of currents, C_x is the x-component of the group velocity C_g, and S is the total of source/sink terms expressed as wave energy density. The right-hand side of the governing equation is represented by three terms, $S = S_{in}+S_{nl}+S_{ds}$ (input by wind, nonlinear interactions, and dissipation, respectively). The dissipation term can be broken into two further terms $S_{ds} = S_{br}+S_{bot}$; the S_{br} term is breaking associated with steepness and instability (whitecapping, surf breaking, etc.); the S_{bot} term includes dissipation due to bottom roughness S_{bf} (friction, scattering), percolation S_{pe}, or non-rigid bottoms S_{mud}. In released versions of SWAN (Holthuijsen et al., 2006), S_{bot} is only associated with rigid seabeds, $S_{bot} = S_{bf}$. The default S_{bf} formula is that of JONSWAP (Hasselmann and Coauthors, 1973), in which the user specifies a simple tuning coefficient that has no apparent physical connection with measurable seabed characteristics. An alternate rigid-bed formula in SWAN is that of Madsen et al. (1988), in which the user specifies a single, representative bedform amplitude at each point in the computational grid on which S_{bf} is estimated.

2.2. Formulae for wave damping by non-rigid bottoms

In this section, three S_{mud} formulae are described; each is a different representation for dissipation by a viscous fluid mud layer. All three formula are so-called "two-layer" models, since they represent the motion of both the mud and water layers; however, they do not all account for viscosity in both layers. These viscous fluid mud models vary in complexity and in assumptions regarding the mud thickness. Analytical models which account for other types of mud behavior—viscoelastic (e.g. MacPherson, 1980; Jiang and Mehta, 1996; Zhang and Ng, 2006) or plastic (e.g. Mei and Liu, 1987)—are not included in this study.

2.2.1. Dalrymple and Liu (1978) formula

Dalrymple and Liu (1978) (henceforth, "DL") propose a formula which represents wave damping due to viscosity in the mud layer and the overlying water layer. It is a relatively accurate approach, since it does not make assumptions about the thickness of the mud layer. It requires a complex iterative solution procedure to compute the dissipation rate. DL also propose a modified form, which they distinguish from the other as a "generally applicable" technique (in their Appendix B), using the assumption that the mud layer is thin, being of the same order of magnitude as the mud Stokes' boundary layer; this thin-layer model also requires iterations.

2.2.2. Ng (2000) formula

The Ng (2000) (henceforth "Ng") formula is a simplification of the DL model. There are two major differences between Ng and DL formulae. Namely, Ng does not require iterations but does require that the mud layer is much thinner than the overlying water layer. Like DL, this model accounts for viscosity in both layers.

Ng provides an expression for the complex wavenumber k. The imaginary part of this wavenumber, k_i gives the wave attenuation rate: $\eta(x,t) = \mathrm{Re}[ae^{i(kx-a)}]$ or for a model of the amplitude decay,

$$a = a_0 e^{-k_i x} \tag{1}$$

where η is the instantaneous free surface elevation and a is the wave amplitude. We implement this in SWAN by considering the case of a single wave train propagating over a flat muddy bottom, using the relation $(\partial/\partial x)(C_{g,x}N)/N = (\partial/\partial x)(C_{g,x}a^2)/a^2$. This gives $S_{bot}/E = -2C_g k_i$ (see also Komen et al. (1994, p. 170)). Fig. 1 shows
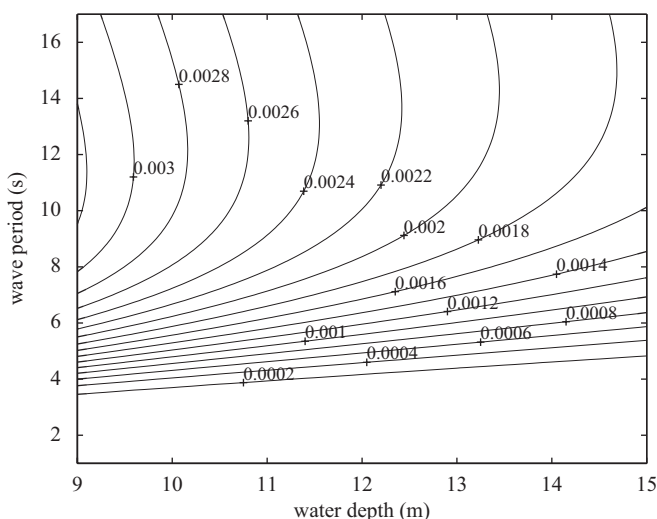
the variation of S_{bot}/E with water depth and wave period given values of density, viscosity, and thickness of mud employed in Section 4. The water depth range (9–15 m) also corresponds to the range for which mud is applied in Section 4.

In this implementation of mud effects in SWAN, a mud-adjusted group velocity is calculated from the real portion of the mud-adjusted wavenumber. Thus, the model can produce "shoaling/de-shoaling" effects associated with spatial variation of mud, separate from traditional shoaling associated with variation of depths. Mud-induced "refraction" has also been added but this effect is not included in the present study.

2.2.3. Winterwerp et al. (2007) formula

Another formula for S_{mud} is given by Winterwerp et al. (2007) (henceforth denoted WDGL); their method of calculating S_{mud} is based on Gade (1958), generalized to non-shallow water depths by De Wit (1995). Like the DL method, and unlike the Ng method, it does not require a thin mud layer and does require iteration to compute the dissipation rate. However, the iteration in the context of a model such as SWAN is not computationally expensive. Unlike both DL method and Ng method, the WDGL method assumes an inviscid water layer. However, dissipation associated with water viscosity is typically quite small.

In WDGL, the method of calculating S_{bot}/E from k_i is different from the implementation of Ng used in this study. WDGL follow Gade's method (Equation II-11 in Gade 1958), which is derived from the energy transport across the water/mud interface, integrated over a wave period, using a number of assumptions and restrictions.

In the version of the Winterwerp et al. (2007) code used herein, the effect of mud on phase and group velocities are not considered.[1]

2.4. Verification of wave damping implementations

Fig. 2 compares the three methods for estimating the dissipation rate D_m ($D_{m/w}$ in the case of DL and Ng), which is the wave attenuation rate due to viscous mud (plus that due to viscous water in the case of DL and Ng), equivalent to the imaginary part of the complex wavenumber, k_i. Variable k_s here is the shallow water real wavenumber, $\sigma/\sqrt{gh}$, used for the normalization consistent with DL. The top and center panels use viscosity, density, water depth, wave period values consistent with Fig. 6 of DL. The DL result is calculated using their "thin lower layer" model. The lower panel uses viscosity, density, water depth, wave period values consistent with Section 4 of the present paper. Horizontal axes of the top and bottom panels are the normalized mud layer thickness, $\tilde{d} = \delta_{m,0}/\Delta_m$, where $\delta_{m,0}$ is the fluidized mud layer thickness and $\Delta_m = \sqrt{2v_m/\sigma}$ represents the Stokes boundary layer thickness.

The negative impact of the thin-layer assumption of Ng is noticeable for normalized mud depths greater than approximately four. For smaller values, the model seems quite accurate. In both the top and bottom panels, the error increases with larger $\tilde{d}$, but at a different rate, suggesting that $\tilde{d}$ may not be the best variable to use when making generalizations regarding the limits of validity of the Ng formula; perhaps $\delta_{m,0}$ or $\delta_{m,0}/h$ would be more appropriate.

The figure shows DL thin model continuing to decrease even for large values of $\tilde{d}$, unlike the Ng model. The top panel shows the DL thin model and WDGL diverging for large $\tilde{d}$. Unfortunately, it is not known which is more accurate in this range. The center panel

Fig. 1. Variation of normalized mud sink term $S_{bot}(\sigma,\theta)/E(\sigma,\theta)$ (in Hz) according to Ng (2000) as implemented herein. Mud thickness $\delta_{m,0} = 40$ cm, mud density $\rho_m = 1310$ kg/m^3, mud kinematic viscosity $v_m = 7.6 \times 10^{-3}$ m^2/s, water density $\rho_w = 1000$ kg/m^3, water kinematic viscosity $v_w = 1.0 \times 10^{-6}$ m^2/s.

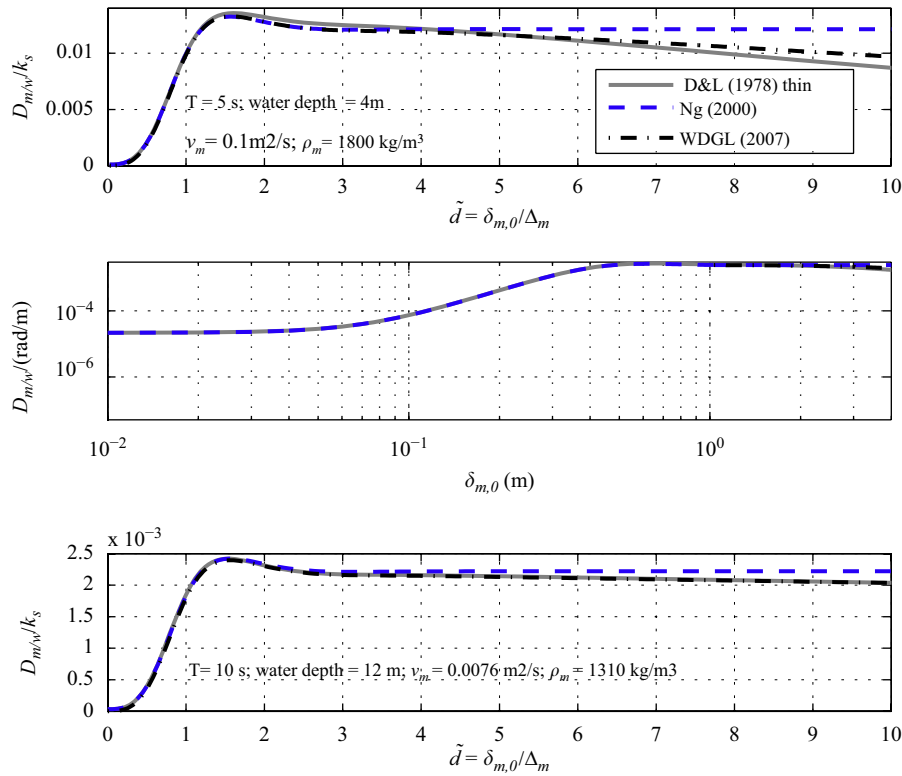[1] Subsequent versions do have this feature (Winterwerp, personal communication).

Fig. 2. Comparison of DL, Ng, and WDGL (2007). Top panel: comparison with DL Fig. 6, normalized dissipation as a function of normalized mud layer thickness; Center panel: as top panel, except on log–log scale, and variables are not normalized. Lower panel: as top panel, but with different settings, chosen to be more representative of the Cassino Beach field experiment.

illustrates the effect of including or omitting the viscosity of the water layer: for small mud thickness values, the WDGL model for D_m deviates from the two $D_{m/w}$ estimates, but this occurs only in a range where the dissipation is very small by any method.

In Fig. 2, top and bottom panels, there exists in each calculation method a value of $\tilde{d}$ for which the dissipation rate is a maximum. There is negligible difference in this value from one calculation method to another: 1.61, 1.57 and 1.57 for DL thin, Ng and WDGL, respectively. This is noteworthy in light of the apparent discrepancy in the literature: Gade (1958) suggests a value of 1.2, while Ng gives 1.55. The text of DL suggests 1.1 to 1.5, but this variation is apparently due to simultaneously using two definitions for "peak value of the damping", only one of which is consistent with our definition.

To verify the implementation of Ng and WDGL formulae in the SWAN model, the expected exponential decay from (1) is compared with the actual decay calculated by SWAN. For the SWAN simulations, settings are identical to those of the lower panel of Fig. 2 (and consistent with Section 4), and all energy is contained in a single frequency/directional bin. This is shown in Fig. 3. The results show that the k_i values calculated by the two methods are very similar. Further, the expected decay rate with the Ng method is identical to the Ng SWAN output. However, the WDGL implementation differs from its corresponding expected decay rate. This is due to the different method of calculating S_{bot}/E from k_i as described above. In separate experiments, it was found that the discrepancy occurs even for shallow water depths, so the shallow water assumption of Gade (1958) is probably not the cause. However, the methods do converge for large wave periods (e.g. $T = 20\,s$). We do not assert that one method is more correct. However, this comparison is crucial when interpreting the results of Section 4 and 5, since it suggests that the increased dissipation with WDGL SWAN versus Ng SWAN in the field application
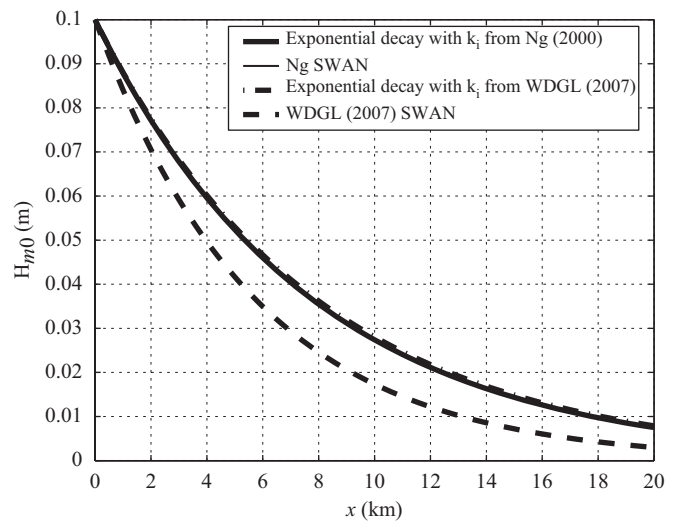

Fig. 3. Comparison of decay rates for Ng (2000) and Winterwerp et al. (2007).

is more likely due to differences in *implementation*, rather than differences between Ng and De Wit (1995).

3. Case study description

3.1. Field site and wave climate

The field site of Cassino Beach (Fig. 4) was chosen due to the long-term presence of a large offshore mud deposit that periodically transports fluid mud throughout the nearshore and
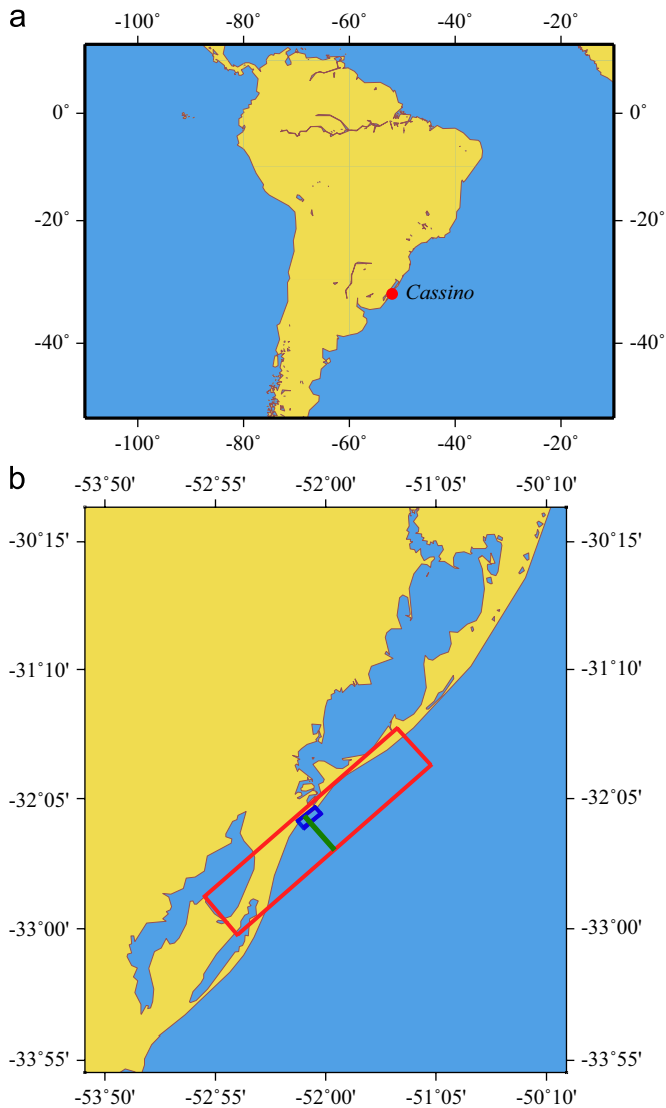
Fig. 4. Map of the study area. Fig. 4a, Geographic location of Cassino. Fig. 4b, Cassino region. Outer SWAN grid shown in red; inner SWAN grid shown in blue; transect used for one-dimensional model shown in green.

sometimes onto the shoreline. A field experiment at the site occurred in May and June 2005. The bathymetry in the vicinity of Cassino Beach is shown in Fig. 5, with locations of wave measuring instruments also shown. The continental shelf slope here is very mild, approximately 25 m vertical over 35 km horizontal. We use four instruments in this study: a Datawell directional waverider buoy at approximately 25 m water depth, a Nortek acoustic Doppler profiler (denoted "NDP") at 8 m, and two pressure gages: "PA" at 6 m and "P5" at 2 m. Description of deployment and operation of the pressure gages can be found in Holland et al., this issue.

The wave climate at Cassino Beach is dominated by windsea and relatively young swells, with peak period of 8–12 s being typical. Time series of significant wave height from the previously mentioned instruments are shown in Fig. 6. Four example directional spectra, derived from buoy data, are also shown in the figure. A large majority of swell fields in the Southern Ocean propagate from the west or southwest. Only the relatively uncommon south-southwesterly swells from the Southern Ocean propagate in the direction of Cassino Beach, which is in fact most typically sheltered from these swells due to the concave shape of the southeastern South American coastline. One large wave event

during the 35-day time period study here occurred on 21–23 May 2005 and was the edge of a fresh swell field generated by a large storm south-southwest of Cassino Beach, east of Argentina and Uruguay. The largest wave event—occurring 16–17 June 2005—is from a small but intense storm just offshore of Cassino Beach.

3.2. Rheology

Based on the measurements during the field experiment (Holland et al., this issue), the initial best estimates of rheology are as follows. Note that even though the experiment data collection capabilities exceeded prior similar attempts, there is considerable uncertainty in these estimates, particularly with respect to natural deviations from measured point samples, therefore an additional estimate of the possible range of values, is given in parentheses:

- total mud layer thickness, $\delta_{m,0,t} = 40$ cm (30–100 cm),
- mud kinematic viscosity, $v_m = 7.6 \times 10^{-3}$ m^2/s (1.4×10^{-3}–15 × 10^{-3} m^2/s),
- mud density, $\rho_m = 1310$ kg/m^3 (1080–1300 kg/m^3),
- water depth where mud is found: $h = 9$–15 m (6–15 m).

Here, the measured total mud layer thickness, $\delta_{m,0,t}$ is given, to distinguish it from the fluidized mud layer thickness, $\delta_{m,0}$, not available from the observations but required for dissipation calculations.

Prior literature has drawn attention to very fast wave attenuation possible due to viscous mud. However, this rate depends heavily on mud characteristics and water depth. To demonstrate this, Table 1 compares dissipation rates and relevant variables for five scenarios, including two previously published works, Gade (1958) and Dalrymple and Liu (1978). For the latter, the example used in DL's discussion of their Fig. 8 is used here. Kaihatu et al. (2007) refers to a manuscript in which the Ng formulation is applied in a phase-resolved model. "Cassino (2005 example)" uses the environmental characteristics taken from observations from the field experiment studied in the present paper, assuming that the entire mud layer is fluidized, i.e. $\delta_{m,0} = \delta_{m,0,t}$. A hypothetical Cassino Beach scenario is presented, identical to the 2005 case except that the mud is located at or near the surf zone. The exponential decay rate is illustrated, here, by showing the distance of propagation at which a wave would be attenuated to 50% or 10% of its original amplitude, indicated as $x_{a=0.5a_0}$ and $x_{a=0.1a_0}$ in the table; this calculation assumes a flat bottom, with no other source/sink terms active (e.g. a low steepness wave with no wind).

It is immediately apparent that the hypothetical field cases used by DL and Kaihatu et al. (2007) shows very fast attenuation relative to either Cassino example. All the three non-Cassino examples have $\tilde{d}$ between 1.1 and 1.6, a range in which the dissipation by mud is expected to reach a maximum value relative to thinner or thicker mud layers. In the Cassino examples, $\tilde{d} = 2.57$, well above this peak; for this value of relative thickness, slightly decreasing the mud thickness would be expected to increase dissipation rate; a large decrease in mud thickness, say to $\delta_{m,0} = 5$ cm, or any increase in mud thickness is expected to decrease the dissipation rate. Also noteworthy is the high viscosity used by DL, 500 times greater than that used for our Cassino application. As expected, in the Cassino example, when the mud is at or near the surf zone, the dissipation is much faster: $x_{a=0.5a_0} = 330$ m compared to 5–6 km with the mud observed further offshore, as it was during the 2005 field experiment.

For the 2005 Cassino example, sensitivities of dissipation level to wave period and water depth are illustrated previously in Fig. 1.
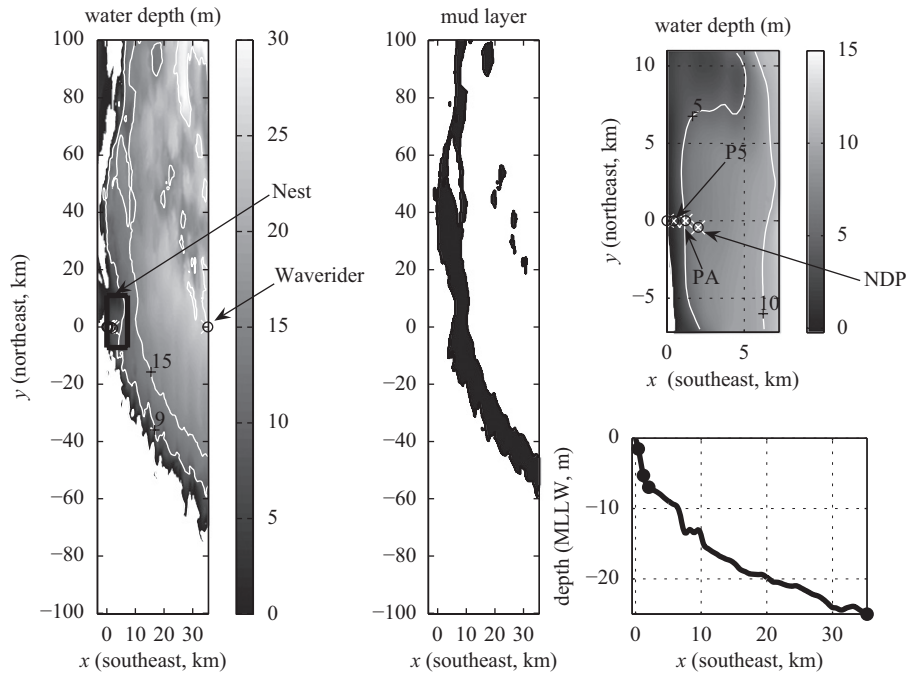
Fig. 5. Bathymetry and mud layer applied in two-dimensional simulations. Left panel: bathymetry on outer SWAN grid, with nest location and buoy location indicated. Center panel: location of applied mud layer in outer SWAN grid. Upper right panel: bathymetry on inner SWAN grid (nest), with horizontal position of wave-measuring instruments shown. Lower right panel: depth profile, from origin to buoy, with P5, PA, NDP and buoy locations indicated.
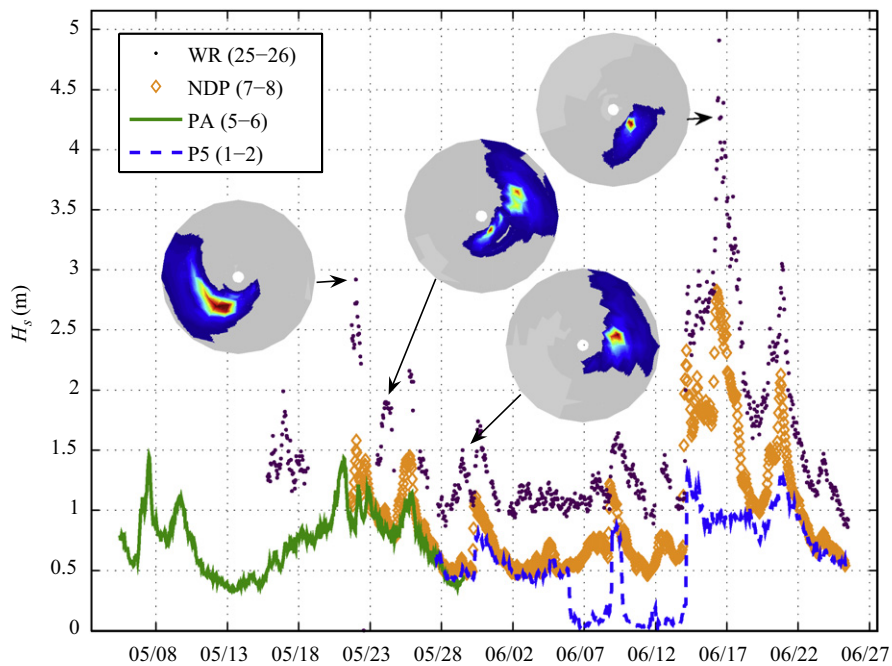

Fig. 6. Time series of significant wave height observed at four locations. "WR" denotes the waverider buoy. Numbers in parentheses are approximate local depths in meters. Directional wave spectra, inferred from buoy data, are also shown, corresponding to four time periods: 0007 UTC 22 May, 0337 UTC 24 May, 1139 UTC 29 May, and 1209 UTC 16 June.

Table 2 illustrates the sensitivity to variation in mud viscosity, density and thickness, using the possible range of values given above. Also included is a calculation for $\delta_{m,0} = 10$ cm, allowing for the possibility that $\delta_{m,0} > \delta_{m,0,t}$. It is apparent that for this wave period and water depth ($T_p = 10$ s and $h = 12$ m), uncertainty in the viscosity is of concern, with decay length scale varying from $x_{a=0.5a_0} = 3.6$ to 12.5 km for the highest and lowest viscosity values, respectively. Further, the computations indicate that if

only a fraction of the mud layer is fluidized, this will also have a large impact. Sensitivity to mud density is relatively minor.

4. Two-dimensional modeling

In this section, we apply SWAN model with and without dissipation by viscous mud. This is performed without any tuning

Table 1
Comparison of dissipation rates and relevant variables for five scenarios

	Gade (1958) Fig. 4	Dalrymple and Liu (1978) Fig. 8	Kaihatu et al. (2007)	Cassino (2005 example)	Cassino (hypo-thetical)
T_p (s)	1.40	5.0	10.0	10.0	10.0
h (m)	0.038	4.0	1.0	12.0	2.0
ρ_m (kg/m³)	1504.00	1800.00	1111.11	1310.00	1310.00
γ	0.57	0.57	0.90	0.76	0.76
ν_w (m²/s)	2.42e-06	2.60e-06	1.00e-06	1.00e-06	1.00e-06
ν_m (m²/s)	2.60e-03	1.49	1.00e-02	7.60e-03	7.60e-03
ζ	32.78	756.26	100.00	87.18	87.18
$\delta_{m,0}$ (m)	0.038	2.0	0.20	0.400	0.400
Δ_m (m)	0.03	1.54	0.18	0.16	0.16
$\tilde{d}$	1.12	1.30	1.12	2.57	2.57
$D_{m/w} = k_i$ (rad/m)	0.90	9.81e-03	7.51e-03	1.29e-04	2.09e-03
$x_{a=0.5a_0}$ (m)	0.77	70.65	92.29	5364	332
$x_{a=0.1a_0}$ (m)	2.56	234.7	306.6	17821	1103

All dissipation rates here are computed using Ng (2000).

Table 2
Sensitivity to mud viscosity, density and thickness, given $T_p = 10$ s and $h = 12$ m, according to Ng (2000)

ν_m (m²/s)	ρ_m (kg/m³)	$\delta_{m,0}$ (m)	$D_{m/w} = k_i$ (rad/m)	$x_{a=0.5a_0}$ (km)
1.4e-3	1310	0.40	5.50e-5	12.5
7.6e-3			1.29e-4	5.4
15e-3			1.94e-4	3.6
7.6e-3	1080	0.40	1.57e-4	4.4
	1310		1.29e-4	5.4
7.6e-3	1310	0.10	4.34e-5	16.0
		0.30	1.36e-4	5.1
		0.40	1.29e-4	5.4
		1.00	1.29e-4	5.4

to improve agreement at the three onshore measurement locations. A total of 431 simulations are used to evaluate trends and sensitivity to forcing conditions, and to generate statistics. The simulations without dissipation by viscous mud help address the objective of evaluating the necessity of (or lack thereof) including physics of wave dissipation by viscous mud in this application. The simulations with dissipation by viscous mud are performed using the Ng SWAN and WDGL SWAN models; these simulations address another objective, which is to, given our best guess of rheology and mud distribution derived from field measurements, evaluate the skill of these models to predict observed wave heights.

Directional spectra for boundary forcing were available for 746 time periods between May 15 and June 25. The process for reducing this population to 431 time periods is summarized now: 14 of 746 boundary spectra were eliminated in quality checking (Section 4.1); 163 of the remaining 732 were discarded due to absence of reliable, coincident wind data (Section 4.2); 46 of the remaining 569 were discarded due to absence of coincident NDP data; 528 time periods were simulated; 97 of these 528 were discarded due to mismatch at the offshore boundary (Section 4.6), leaving 431 time periods for calculation of statistics.

4.1. Boundary forcing

The wave model's outer computational grid is designed such that the center of the offshore boundary corresponds to the location of the Datawell Waverider buoy, from which directional measurements are available for the time period of interest.

Directional data were provided in the form of five variables given at each of 64 frequencies non-uniformly spaced from 0.025 to 0.58 Hz. The five variables are spectral energy density and four directional moments describing the unmeasured normalized directional distribution for that frequency, $D(\theta)$. This information was available for 746 time periods between May 15 and June 25. The procedure for estimating $D(\theta)$ is as follows: The four Fourier coefficients corresponding to these four moments were calculated directly. Then, an estimate of $D(\theta)$ was calculated using the maximum entropy method (Lygre and Krogstad, 1986). In the case of 14 spectra, the integrated spectra did not match the waveheight in the header of the data file; these were discarded. Thus, 732 $E(\sigma,\theta)$ estimates were retained and converted to a format readable by SWAN.

4.2. Wind forcing

Wind vectors were estimated using high-frequency energy measured by the waverider buoy. For each of 732 spectra, the wind speed is chosen that, in fetch-limited conditions, results in a SWAN-predicted high-frequency spectrum consistent with the measured spectrum. This algorithm was able to create a relatively confident prediction for 569 of 732 cases. The algorithm is described in Appendix A.

4.3. Bathymetry and water level specification

Regional charts, ship surveys, digitized shorelines, and nearshore bathymetry from a jet-ski system were used to compute the bathymetric surface used in the model. The data were corrected to remove tidal offsets and merged using the method of Plant et al. (2002). The nearshore surveys were made during late April and May 2005. See Holland et al. (this issue) for further description.

The tide range at Cassino Beach is approximately ± 60 cm from the mean water level, with a significant meteorological component. Bathymetry is relative to mean lower low water; thus, an offset is determined for each hindcast using pressure gage data. For the period 26 May–24 June, "P2" in approximately 1.2 m water depth, corrected for barometric pressure, is used. Prior to 26 May, the "PA" gage is used, also used in the wave comparisons below.

4.4. Mud specification

For the two-dimensional application of the Ng SWAN, we used the mud-related variables given of the initial best estimate [$\delta_{m,0} = 40$ cm, $\nu_m = 7.6$e–03 m²/s, $\rho_m = 1310$ kg/m³, as described in Section 3.2]. For the horizontal location, the mud is applied where the water depth is between 9 and 15 m (see center panel in Fig. 5). In locations where mud is not applied, the source term S_{bot} is assumed zero. In other words, bottom friction associated with sand or otherwise rigid seafloor is not included. This is motivated

by lack of measurements describing possible rigid bedforms. (Separate simulations with dissipation by rigid bed forms via Madsen et al. (1988) were produced; these results are not presented here, but are discussed in Section 6.)

4.5. Grid specification, wave generation physics

An inner nest was included in the simulations to provide higher resolution in the nearshore; the nest position is shown in Figs. 4b and 5. Additional details on the model design are as follows:

- a rotated rectilinear grid, such that the positive x-direction is $48.33°$ clockwise from the west-to-east direction,
- for the x-axis, shore-normal and positive in the southeast direction, the grid spacing $\Delta x = 252$ m, with 155 grid nodes (and for the inner nest, 50 m and 146 nodes),
- for the y-axis, shore-parallel and positive in the northeast direction, the grid spacing $\Delta y = 500$ m, with 402 grid nodes (and for the inner nest, 50 m and 365 nodes),
- in frequency space, 34 bins in logarithmic distribution from 0.0418 to 1.0 Hz,
- $10°$ directional resolution (36 directional nodes),
- stationary computations, with default settings for numerics,
- default settings for nonlinear interactions S_{nl4} and depth-limited breaking $S_{ds,br}$,
- for whitecapping term, $S_{ds,wc}$, the van der Westhuysen et al. (2007) formula is used to reduce problems associated with non-physical dependence on mean steepness (Rogers et al., 2003 and references therein), and
- for wind-to-wave energy transfer term, S_{in}, the Yan (1987) formula is used (see van der Westhuysen et al. (2007)).

4.6. Computations and Results

Five hundred and twenty eight two-dimensional simulations with each of the three SWAN variants were performed ($S_{bot} = 0$, $S_{bot} = S_{mud}$ according to Ng, and $S_{bot} = S_{mud}$ according to WDGL). Simulations were discarded if any of the three models produced a mismatch of wave height at the offshore boundary (greater than 4% normalized error), indicative of problems with wave growth internally.[2] Ninety seven time periods were omitted, leaving 431 cases. Results for two-dimensional simulations are shown in Fig. 7 and Table 3. Statistics shown in the table are: number of comparisons, bottom-induced dissipation applied, bias, rms error, correlation coefficient, standard deviation of error (i.e. rms error with bias effect removed), scatter index, and the mean of observed values. The scatter index is defined as (e.g. Cardone et al. 1995)

$$SI = \frac{rmse}{\bar{O}}$$

and correlation coefficient is

$$CC = \frac{\overline{(O - \bar{O})(M - \bar{M})}}{\sqrt{\overline{(O - \bar{O})^2}}\sqrt{\overline{(M - \bar{M})^2}}}$$

where overscore indicates a mean, O are observations and M are model values.

It is apparent in the comparisons for P5 that a distinct sub-population exists for which observed waveheights are very small

(less than 38 cm) and much smaller than waveheights from either of the two models. These correspond to two intervals during June 6–15. It was determined that the small waveheights are very likely due to instrument failure (the gage may have been covered by sediment) and therefore these points are not included in the calculated statistics.

For the simulations without mud-induced dissipation (left column in Fig. 7), there is a clear trend of overprediction of wave energy, with bias of 33, 46, and 16 cm at NDP, PA and P5, respectively. This addresses one of the previously stated objectives, insofar as it suggests that some type of bottom-induced dissipation is needed for accurate prediction of the nearshore energy level. Implied in this conclusion is the assumption that there is no other source of error—in the observations or simulations—that would lead to large positive bias; possible errors are discussed in Section 6. A surprisingly small bias exists for the high-energy simulations without mud-induced dissipation. In fact, there is little or no bias for the time periods with largest waveheight in the NDP and P5 records. One possible explanation is that the viscosity could be reduced under stronger level of forcing, as might be expected with a thixotropic (shear-thinning) fluid. Or, the water/mud interface may be indistinct during high energy events, e.g. due to sediment suspension, preventing effective energy transfer.

In the simulations with mud-induced dissipation (right column in Fig. 7), the positive bias is eliminated. At the two shallower locations, PA and P5, the bias with the Ng model is very small relative to the $S_{bot} = 0$ simulations (−6 and −8 cm, compared to +46 and +16 cm). At the NDP location, the bias is similar, but of opposite sign (−29 cm compared to +33 cm). The negative bias at this location suggests that the modeled dissipation is too strong in the region between the NDP and the waverider buoy, with the implied assumption as noted above. One explanation is that the true mud distribution in this region might be more thin, patchy, or less fluidized than the uniform lens of 40 cm fluid mud applied here; this is explored further via inverse modeling in Section 5. The rms error and scatter index are mostly improved by including S_{mud}, while the correlation is not always improved; in fact, it is significantly worse at PA.

Comparing the Ng and WDGL statistics, it is clear that the dissipation is generally stronger with the latter. Considering the comparisons in Section 2, this is most likely due to difference in implementation rather than in the formulae themselves.

5. One-dimensional modeling: forward and inverse solutions

In the above-mentioned two-dimensional modeling, the model with $S_{bot} = 0$ tends to overpredict wave energy and the models that include S_{mud} tend to underpredict energy. Assuming that modeling errors unrelated to S_{bot} are relatively small, this result suggests that the wave dissipation S_{mud} occurred at Cassino but is overpredicted by the model if the calculations are made using mud characteristics based on field measurements (Section 3.2). The range of uncertainty in the measured mud viscosity and the thickness of the fluidized mud layer (Table 2) are not small, and the mud distribution shown in Fig. 5 is unlikely to be an accurate portrayal of the heterogeneity of the actual mud deposits. Further, the mud distribution, thickness, and depth of fluidization may not have been constant during the simulation period; core samples—which in fact only identified the first two of these three variables—were taken during only one week of May 2005. The dissipation calculations given in Table 2 suggest that the model results could be sensitive to these uncertainties in the forcing.

One method of quantifying the sensitivity of the results to the uncertainty in forcing is to run the forward model with a number

---

[2] This is a surprising result, since the wind speed inference algorithm should provide the optimal wind speed for producing in the model the same wind sea as observed at the buoy. This is due to non-physical sea–swell interaction and is discussed further in the Appendix A.
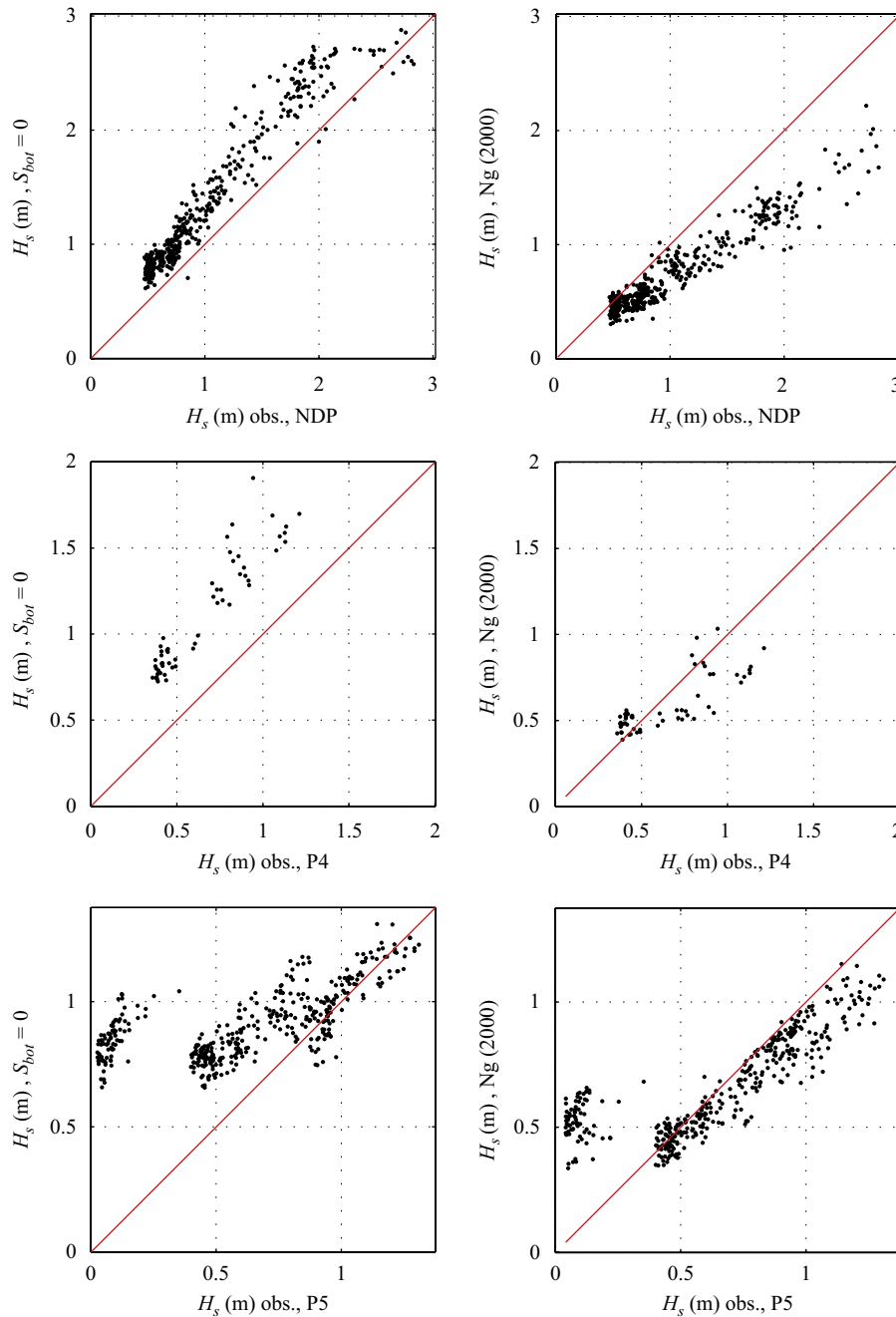
Fig. 7. Scatter plot comparison of SWAN vs. observations at three locations, both with and without dissipation by viscous mud included in SWAN (Ng formula).

of forcing conditions and compare the results. However, due to the non-monotonic behavior evident in Fig. 2, a large number of hypothetical conditions would be required to quantify the sensitivity. A more deterministic approach is preferred. To this end, inverse modeling was used to determine if any mud distribution would yield the observed waveheights, and if so, what that distribution is. (Sensitivity to uncertainty in viscosity was also explored in this manner; these results are discussed qualitatively in Section 6.)

The forward modeling was a blindfold process, so the NDP, PA, and P5 wave observations were disregarded until the comparison stage. Similarly, the inversion for the mud distribution does not utilize much of the relevant knowledge obtained from the mud observations. Most importantly, the inversion for mud distribution permits solutions suggesting mud

at locations shallower than the 9 m depth contour, which is not consistent with existing observations. Correspondence, or lack thereof, between the inversion results and the mud observations provides insight unavailable from the forward modeling alone.

Inverse modeling requires multiple simulations for each of the time periods, so creating inverse solutions for each of 431 time periods might normally require more computation time than is practical. This challenge was addressed by reducing the two-dimensional simulations to one geographic dimension, specifically a cross-shore transect running from the waverider buoy to the shoreline. Of course, by ignoring long-shore variation in the system, some error is introduced, so in Section 5.2 below, the forward two-dimensional model is compared with the forward one-dimensional model.

Table 3
Significant wave height statistics for two-dimensional simulations

	n	S_{bot}	Bias (m)	rmse (m)	CC	stde (m)	SI	⟨obs⟩ (m)
WR	431	0	0.01	0.04	1.00	0.03	0.02	1.72
		Ng (2000)	0.01	0.03	1.00	0.03	0.02	–
		WDGL	0.01	0.03	1.00	0.03	0.02	
NDP	431	0	0.33	0.37	0.97	0.17	0.36	1.03
		Ng (2000)	−0.29	0.38	0.96	0.25	0.37	–
		WDGL	−0.40	0.51	0.94	0.31	0.49	
PA	55	0	0.46	0.48	0.94	0.13	0.74	0.65
		Ng (2000)	−0.06	0.17	79	0.17	0.27	–
		WDGL	−0.12	0.20	0.81	0.16	0.31	
P5	323	0	0.16	0.22	0.84	0.15	0.29	0.76
		Ng (2000)	−0.08	0.11	0.95	0.09	0.15	–
		WDGL	−0.15	0.18	0.93	0.09	0.24	–

Table 4
Significant wave height statistics for one-dimensional simulations

	n	S_{bot}	Bias (m)	rmse (m)	CC	stde (m)	SI	⟨obs⟩ (m)
WR	431	0	0.02	0.05	1.00	0.05	0.03	1.72
		Ng (40 cm)	0.02	0.05	1.00	0.04	0.03	–
		WDGL (40 cm)	0.02	0.05	1.00	0.04	0.03	–
		WDGL (1 m)	0.02	0.05	1.00	0.04	0.03	–
		WDGL Inverse	0.02	0.05	1.00	0.04	0.03	
NDP	431	0	0.36	0.41	0.96	0.19	0.39	1.03
		Ng (40 cm)	−0.22	0.31	0.96	0.22	0.30	–
		WDGL (40 cm)	−0.32	0.42	0.94	0.28	0.41	–
		WDGL (1 m)	−0.31	0.41	0.94	0.27	0.39	–
		WDGL Inverse	−0.02	0.03	1.00	0.02	0.03	
PA	55	0	0.52	0.55	0.92	0.18	0.85	0.65
		Ng (40 cm)	0.01	0.16	0.77	0.17	0.25	–
		WDGL (40 cm)	−0.04	0.17	0.79	0.16	0.26	–
		WDGL (1 m)	−0.03	0.16	0.80	0.16	0.24	–
		WDGL Inverse	0.01	0.03	1.00	0.02	0.04	
P5	323	0	0.15	0.22	0.79	0.16	0.29	0.76
		Ng (40 cm)	−0.06	0.10	0.95	0.08	0.13	–
		WDGL (40 cm)	−0.12	0.14	0.95	0.08	0.18	–
		WDGL (1 m)	−0.11	0.13	0.95	0.08	0.17	–
		WDGL Inverse	−0.02	0.04	0.99	0.04	0.06	–

5.1. One-dimensional grid specification

Model design choices differing from the two-dimensional simulations are as follows:

- For the *x*-axis, shore-normal and positive in the southeast direction, the grid spacing $\Delta x = 50$ m, with 771 grid nodes (no inner nest).
- There is no shore-parallel *y*-axis.
- A curvature-based stopping criterion is used, thus typically computing more iterations than would be the case if the default criterion was used. This potentially improves accuracy, see Zijlema and van der Westhuysen (2005).

5.2. Forward model results

Table 4 compares the one-dimensional forward model results for several models:

- no dissipation by mud,
- dissipation by mud with 40 cm mud layer thickness applied between 9 and 15 m water depth contours using Ng SWAN,
- dissipation by mud with 40 cm mud layer thickness applied between 9 and 15 m water depth contours using WDGL SWAN,
- dissipation by mud with 1 m mud layer thickness applied between 9 and 15 m water depth contours using WDGL SWAN, and
- inversion results, with mud thickness adjusted to retrieve observed wave heights.

Statistics for the two-dimensional and one-dimensional simulations can be compared in Tables 3 and 4. It is apparent that there are some differences between the one- and two-dimensional results, but none that would actually change the conclusions. The most noteworthy difference is in the bias of Ng SWAN at PA, which changes from small negative bias in the two-dimensional case (−6 cm) to slightly positive in the one-dimensional case (+1 cm).

Knowing that application with $\delta_{m,0} = 40$ cm results in too much dissipation (i.e. positive wave height bias), it is useful to consider whether application with $\delta_{m,0} = 1$ m will improve this bias. For a typical boundary layer thickness value, say $\Delta_m = 16$ cm (Table 1), the mud thickness of $\delta_{m,0} = 40$ cm $> 1.6\Delta_m$. Referring to Fig. 2, this suggests that increasing the mud thickness will result in a decrease in dissipation and, therefore, improve the negative bias seen for the 40 cm WDGL set in Table 4. However, the bias for the 1 m WDGL set is only slightly better (for NDP, a change from −29 to −28 cm), indicating that the dissipation in this thickness range is only weakly sensitive to mud thickness (consistent with Fig. 2), and zero bias cannot be achieved without using a fluidized mud layer thickness $\delta_{m,0}$ which is less than the probable range of total mud thickness ($\delta_{m,0,t} = 30$ cm–1 m, Section 3.2) or a smaller mud viscosity.

5.3. Inverse modeling method description

Given the uncertainties in the forward modeling outlined above, an inversion methodology was developed. The inversion is simple: the shore-normal transect which constitutes the computational grid is split into zones, and working in a shoreward direction, the mud layer thickness is determined which results in the wave height that was observed at the shoreward end of each zone. The zones are as follows:

(1) Zone A, from the offshore boundary to 15 m water depth. It is assumed that no mud exists here, $\delta_{m,0} = 0$.
(2) Zone B, from 15 m water depth to 7.3 m depth, terminating at NDP.
(3) Zone C, from 7.3 to 5.6 m depth, terminating at PA.
(4) Zone D, from 5.6 to 1.8 m depth, terminating at P5.
(5) Zone E, from 1.8 m depth to the shoreline: $\delta_{m,0} = 0$ assumed, but dissipation level in this zone is actually irrelevant to the tabulated model-data comparisons, since waves are not measured after they pass through this zone.

In cases where PA data are not available, Zones C and D are combined and inversion for the two zones is based on waveheight at P5. In cases where P5 data are not available, Zone D is treated similar to Zone E, i.e. $\delta_{m,0} = 0$ assumed.

One inherent assumption in the inversion is that the waveheight as an observation point is affected only by the mud offshore of that point, e.g. the waveheight at NDP is not affected by the mud, or lack thereof, in Zone C. This assumption allows the procedure to advance in a stepwise fashion, from Zone B to C to D, rather than solving all three simultaneously. Since the slope is

very mild, and there are many cases with windsea propagating toward deeper water (i.e. offshore winds), this assumption is not obviously valid. The underlying physical assumption is that these fetch-limited waves are too short to induce significant pressures near the bottom and, therefore, induce motion in the mud layer. The validity of this assumption is discussed further in Section 5.4.

Based on the similarity of the two models in the previous results, there was no compelling reason to perform the inversion for both Ng SWAN and WDGL SWAN. The latter was chosen for the inversion, since that model is valid for a larger range of mud thickness (Fig. 2).

An inverse solution is possible when the observed wave height is bounded by the result with zero mud and the result with most dissipative possible mud thickness: $H_{\delta_{m,0,\max}} < H_{obs} < H_{\delta_{m,0}=0}$. The thickness $\delta_{m,0,\max}$ typically corresponds to $1.5 < \tilde{d} < 1.6$. i.e. $\delta_{m,0,\max} \approx 1.5 \Delta_m$ in our applications of WDGL and Ng. The relationship of dissipation (and therefore, waveheight in the inversion) with mud thickness always has a single peak (trough). Thus, when one solution exists, there is always one other solution. This is illustrated in Fig. 8, where the horizontal line represents the observed waveheight that the inversion should produce. Since the lines intersect, there exists a pair of solutions: one solution exists at $\delta_{m,0,x} \approx 7$ cm and another at $\delta_{m,0} \approx 11$ m. It is apparent that in the thick region (which is the right-hand side of the figure, corresponding to $\delta_{m,0} < 1.5 \Delta_m$), the dissipation, and therefore the resulting waveheight, is only weakly sensitive to the mud thickness. When two solutions exist, the procedure must choose one. In the present implementation, the inversion always chooses the thinner solution, since the thicker solution was often unrealistic, as in this example ($\delta_{m,0} = 11$ m). The waveheight from the forward model is not a linear function of mud thickness; thus, the problem must be solved via an iterative sequence of forward simulations. The solid line in Fig. 8 shows the waveheight from many (119) applications of the forward model, each using a different mud thickness. In practice, this many forward model runs is not necessary; rather, a modified Newton–Raphson procedure is used to find the solution within a relatively small number of forward simulations. When the problem is not bounded (i.e. the inversion cannot match the observed waveheights exactly, which would be the case if the two lines in Fig. 8 did not intersect) the solution is used which yields the smallest waveheight mismatch; specifically when $H_{\delta_{m,0,\max}} > H_{obs}$, $\delta_{m,0} = \delta_{m,0,\max}$ and when $H_{obs} > H_{\delta_{m,0}=0}$, $\delta_{m,0} = 0$.

5.4. Inverse model results

The inversion solution yielded an exact match in waveheight in *all* zones for over half (248) of the 431 cases. In the other cases, the error-minimizing solution typically yielded excellent model-data agreement: scatter plot comparisons (not shown) and statistics (included in Table 4) reflect this.

The inferred mud thickness values for the three zones are shown in Fig. 9. These values are consistently smaller than the observation-based estimate (40 cm). This is not unexpected, since in the blindfold applications, the dissipation is overpredicted using $\delta_{m,0} = 40$ cm, e.g. a -32 cm waveheight bias at NDP in the one-dimensional WDGL set. The smaller mud thickness given by the inversion might be interpreted to mean that only the upper portion of the mud is fluidized.

The Zone B solution via NDP is fairly stationary for the entire 35-day period, at $\delta_{m,0} = 7$–10 cm, while the Zone C and D solutions are less so; for example, the solutions based on P5 are stationary only for 5–10 days at a time. There is similar variability in the solutions based on waveheights observed at PA. If this variability is not the result of model or instrumentation error, it suggests that the mud layer is more dynamic than the infrequently sampled data. Such variability could be associated with sediment transport or time-variation of the depth of fluidization of the mud layer. Further, the inversion suggests a fairly consistent non-zero S_{bot} in the region shoreward of the 9 m contour, where field observations do not suggest the presence of mud.

An assumption discussed above—that the waveheight at an observation point is affected only by the mud offshore of that point—appears to be vindicated, since the resulting mud solutions match observed waveheights very well. For example, the inversion solves for the mud thickness in Zone B, gets a match to observed waveheights at NDP, progresses to and creates a solution for Zone C, and this modification of the mud thickness in Zone C does not result in degraded agreement at the gage at the deeper end of this zone, NDP.

6. Discussion

6.1. Modeling errors

As noted already, many of our conclusions require that, in the simulations with $S_{bot} = 0$, this omission is the dominant source of error. Further, it is obvious that the mud thickness values
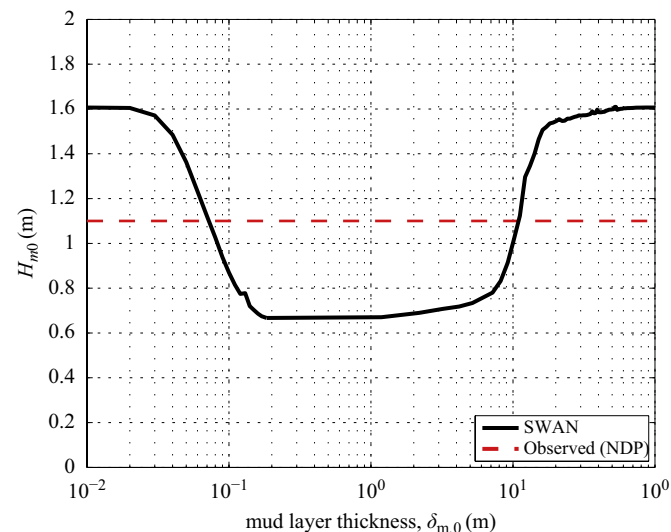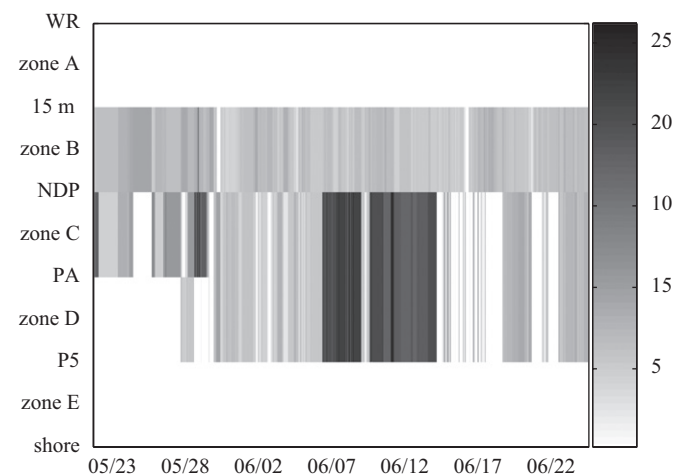

Fig. 8. Example of inferring mud thickness from wave height observation. Here, solutions of $\delta_{m,0} = 0.07$ and 11 m are obtained. In this case, the maximum dissipation occurs with $\delta_{m,0,\max} = 18.4$ cm.

Fig. 9. Inferred time series of mud thickness in cm. This shows the solution in terms of $\langle \delta_{m,0}, x, t \rangle$, with $\langle \rho_m, v_m \rangle$ held constant.

determined by the inversion are affected by all errors inherent in the modeling and measurements. Thus, it is useful to characterize—and if possible, estimate—this error. Model error is caused by error in forcing, omissions in forcing, errors in approximations for physical processes, omission of physical processes, model simplifications, and numerical error. Error associated with uncertainty in a type of forcing—the specification of the thickness and distribution of the liquefied mud layer—was addressed in Section 5. In this section, other types of errors are discussed.

Omission of the longshore coordinate in the inversion is one example of a model simplification which certainly produces error. However, this error is readily estimated from comparison of Tables 3 and 4 and appears to be modest. Measurement error is another concern; however, since we are dealing primarily with a low-order moment, waveheight, instrument error is expected to be small: less than 15% random error and without systematic bias as long as the instrument is functioning properly. Error in bathymetry is another possible source of error. The bathymetry in the nearshore (depths less than 2 m) can be expected to vary in time due to sediment transport. Jet-ski surveys (Holland et al., this issue) showed no appreciable change during May 2005, but were unfortunately not conducted during June 2005; this uncertainty is relevant to model-data comparisons at the "P5" location during this period.

Spatially varying currents cause waves to refract and shoal/ strain in a manner similar to spatially varying water depth. Further, opposing currents can cause waves to steepen, making them more likely to break. Wave–current interaction is not considered in the presented simulations. Due to the Patos Lagoon inlet only 5–10 km to the northeast of Cassino Beach, surface currents in this area are significant. On a day with high river discharge, the surface currents in the jet from this inlet can easily exceed 1 m/s (Vinzon et al., this volume). If this jet is straight, and assuming linear waves, the waves will be refracted inside the jet, but will leave the jet with their original characteristics, and thus currents inside the jet would not necessarily affect waveheights at the instrument locations. However, the currents outside the jet are also quite large, sometimes reaching 0.5 m/s, with a recirculation pattern toward the northeast observed at times. A typical group velocity of a wave at the spectral peak, say $T = 10$ s, using 15 m water depth, is 9 m/s. This circulation would have some effect on the local energy level of such a wave via refraction and straining, but not a large effect. For shorter waves, the group velocity is smaller, e.g. 2.5 m/s, and the effect of currents could be dominant; however since these waves are typically in the spectral tail, this does not necessarily imply a dominant effect on the total energy (waveheight). Therefore, we believe that currents are not a major source of error.

Another potential source of error is the assumption of uniform wave conditions along the offshore boundary, prescribed equal to the spectra observed by the waverider buoy. Spatial variability of swell fields is probably not a problem, since swell fields tend to be much larger than our outer grid. However, since our offshore boundary is not in deep water, there will certainly be some variation of wave conditions along the boundary associated with shoaling, refraction and non-conservative processes such as bottom friction and breaking. Sensitivity to this error was estimated by running a regional scale model, initialized in deep water, with output along the offshore boundary of our subregional scale model. This test was performed separately for swells approaching from the south (shore-oblique), southeast (directly onshore), and east-northeast (shore-oblique). In the case of waves approaching from the south, our assumption of uniform boundary conditions is estimated to result in 20% overprediction of waveheight. For swells from the southeast, there is no error (since waves at the nearshore gages are coming from the direction

of the buoy), and for waves from the east-northeast, a small underprediction (5%). Comparing bias of the $S_{bot} = 0$ model at the NDP location versus the dominant wave direction, there is not a clear correlation, suggesting that this effect is not particularly important.

Elastic behavior of the mud, not included in the viscous models used here, can either increase dissipation, especially via resonance (see Zhang and Ng, 2006), or decrease dissipation by restraining the motion of the bed (see MacPherson, 1980; Hsiao and Shemdin, 1980). One can speculate that the apparent overprediction of dissipation by either S_{mud} formulation used here is due to this omission. Unfortunately, without actually estimating the elasticity of the mud at Cassino Beach and performing calculations, it is not possible to say whether including this process would increase or decrease estimated dissipation. Implementing the formula of Zhang and Ng (2006) in SWAN is a potential avenue for further work. Treatment of the mud as a plastic is yet another option (e.g. Mei and Liu, 1987). In any event, viscous fluid mud, visco-elastic mud, plastic mud, and rigid mud may have coexisted at the field site, in layers. In the forward model applications, it is assumed that the entire mud layer is liquefied. As shown in Section 3.2, if only a small portion of the mud layer, say the upper 10 cm, is liquefied, this would tend to reduce dissipation. Thus, this is another possible explanation for overpredicted dissipation with the forward models.

Due to lack of knowledge regarding sand bedforms on this beach, bottom friction is not applied in the simulation in areas where mud thickness is zero. This omission could account for some of the underprediction of dissipation shoreward of the 9 m contour suggested by the inverse modeling, but we do not believe that the bedforms—if they existed at all—were large enough to play a major role. This is discussed quantitatively in Section 6.3.

6.2. Relative importance of depth-limited breaking

Though not included here, comparisons were made to a SWAN model implementation with depth-limited breaking disabled. These model results suggest surf breaking is only significant shoreward of the PA location and only during the higher wave events. This is consistent with traditional rules of thumb regarding maximum height to depth ratios (e.g. Dean and Dalrymple, 1991). Thus, breaking is only relevant to the comparisons at the P5 location, and then only for a few time periods. The comparison suggests that during the June 16–17 high wave event, surf breaking plays a *dominant* role in the P5 comparisons. In fact, at this location the highest waves do *not* occur during June 16–17, but during periods prior and after, June 14 and June 20 when breaking was apparently reduced. Encouragingly, this behavior is seen both in the observations and in the model that includes surf breaking.

6.3. Application with sandy bed

It was determined in Section 4 that inclusion of dissipation by wave-mud interactions S_{bot} greatly improved bias statistics, especially at gages PA and P5. The question might be asked, "Could the same improvement be achieved by using a formula for S_{bot} based on a sandy seabed?" Such a study was in fact performed. Specifically 171 two-dimensional simulations from Section 4 were applied using the Madsen et al. (1988) formula for dissipation by bedforms. Since there was no observation-based guidance, a bedform amplitude of 5 cm was applied uniformly over the domain. Interestingly, these results show a similar improvement in bias compared to the case with S_{mud}. Comparing the statistics with mud dissipation versus those with sand

dissipation, they were fairly similar, with the former being moderately better at P5 and the latter slightly better at NDP and PA. However, the similarity of magnitude of the mud-based and sand-based dissipation is only due to the application of the sandy bedforms over a larger area.

The actual decay rate based on Madsen et al. (1988) with 5 cm bedform amplitude is considerably smaller than that of Ng as applied in Section 4. Unfortunately, comparison of the decay rate based on Madsen et al. (1988) with those in Table 1 is not straightforward, because this source term is nonlinear, meaning that the exponential decay rate of the wave amplitude is dependent on the amplitude itself. But to provide an example, in the case of $h = 12$ m in Table 1, if we use a waveheight of 1 m and a bedform amplitude of 5 cm, the decay rate $k_i = 3.5 \times 10^{-5}$ rad/m compared to $k_i = 1.3 \times 10^{-4}$ rad/m using Ng with stated mud characteristics.

6.4. Inversion for additional variables

This inversion described above assumes constant, uniform values for the mud density and viscosity, $\rho_m = 1310$ kg/m^3, and $v_m = 7.6 \times 10^{-3}$ m^2/s, both based on rheometry. Only the mud thickness and—in a limited fashion—the horizontal (x) distribution are unknowns to be solved for. Thus, the mud thickness being solved is $\delta_{m,0} = \delta_{m,0}(x,t)$ and the outcome of the inversion is the solution set in terms of $\langle \delta_{m,0}, x, t \rangle$. However, as noted in Section 3.2, there is also a range of uncertainty in the mud viscosity and density, so the solution set might be more generally in terms of $\langle \delta_{m,0}, v_m, \rho_m, x, t \rangle$. An obvious question is, "If we had used a different mud viscosity, within the range of probable values, would we have recovered mud thickness values closer to the observation-based estimate (40 cm), instead of 20 cm?". To repeat the inversion process for multiple possible values of ρ_m and v_m—say ten values each—would increase the total computational requirement by a factor of 100. However, this is not strictly necessary. Instead, for each $\langle x,t \rangle$, we can use the WDGL formulation to calculate k_i from $\delta_{m,0}$ given the $\langle v_m, \rho_m \rangle$ values used in the actual inversion and then apply the formulation again to calculate combinations of $\langle \delta_{m,0}, v_m, \rho_m \rangle$ that produce this k_i. None of this requires new computations with the wave model. Application of the WDGL formulation in this manner does require a representative value of wave period T, so it is only an approximate solution, but the outcome appears to be only weakly sensitive to variations in the chosen values for T.

7. Summary and conclusion

Dissipation by viscous mud by two formulations was independently implemented in SWAN: (1) De Wit (1995) in Winterwerp et al. (2007) and (2) Ng (2000) herein. Both are applied to the Cassino Beach 2005 field experiment. Calculations with the Ng formula reveal that—though this is a clearly muddy area—dissipation by mud in this field experiment is weak relative to examples given in the literature, as well as a hypothetical scenario where the mud is at/near the surf zone in Cassino, such as occurs there periodically. Calculations also suggest that the uncertainty in the specification of the mud in the modeling exercise is likely to have significant impact on results. Uncertainty in viscosity and fluidized mud thickness are found to be particularly important. Further, the strong sensitivity of dissipation to the local water depth implies that the modeling is highly sensitive to errors in the horizontal distribution of the mud.

The two formulations are compared herein. There are two primary differences. First, the Ng formula is intended only for cases where the mud layer is thin relative to the overlying water layer, and it is shown here that the WDGL implementation has a broader range of validity. However, the thickness of the mud in the Cassino Beach application does appear to be well within the limits of validity of the Ng formula. The second major difference is the method of converting the exponential decay rate k_i into a spectral dissipation term S_{bot}; the methods predict similar k_i for the case study, but S_{bot} is significantly larger with the Winterwerp et al. (2007) method.

In the Cassino Beach 2005 application of the wave model with $S_{bot} = 0$ (i.e. no dissipation by wave-bottom interaction), wave energy is overpredicted at all three measurement locations. Assuming that other sources of systematic error are small, this overprediction of energy suggests an underprediction of dissipation. This trend is quite consistent for the 35-day period studied, with the only exception being during a single high energy wave event. During this time period, the waveheight is well predicted using $S_{bot} = 0$. Two possible explanations are suggested: (1) the water/mud interface may have been obliterated by sediment suspension during the high wave event, or (2) the mud may be thixotropic, i.e. reduced viscosity under greater wave forcing.

At all other time periods, application of $S_{bot} = S_{mud}$, with mud thickness, horizontal distribution and rheology based on observations, results in modestly underpredicted wave energy for both dissipation formulations applied, suggesting that the dissipation may be overpredicted. We offer three speculative explanations for this. First, the utilized models assume zero elasticity; we point out that the use of non-zero elasticity might improve results by reducing the predicted dissipation (e.g. see MacPherson, 1980). Second, the actual mud was certainly less uniform than as applied in the model; thus, it might have been significantly thinner in places. Third, there is a very strong possibility that only the top portion of measured mud was fluidized.

The forward modeling methodology described above is potentially useful in wave hindcasting and forecasting, if the rheology and mud distribution are known with some degree of confidence. In the reverse situation, the waves are measured and the mud is poorly described. A method of inferring mud distribution from observed wave height distributions is presented. In application of this method, the observed wave heights are successfully recovered by the inversion. The optimal thicknesses showed both spatial and temporal variability suggesting that more detailed observations of these difficult parameters are necessary to properly validate dissipation mechanisms.

Appendix A. Wind vector algorithm

Two sources were initially available to provide time series of wind vectors for the time period of the field experiment: an anemometer located near Cassino Beach, and the Navy's

operational global atmospheric model, NOGAPS (Hogan and Rosmond, 1991). Comparing these two, the wind directions were consistent, but the anemometer wind speeds and the NOGAPS winds speeds over a nearby land point (53°W, 32°S) were systematically lower than the NOGAPS wind speeds over a nearby sea point (52°W, 33°S), presumably due to land frictional effects. Direct use of the anemometer winds was ruled out due to this apparent bias. There was concern that temporal structure of the NOGAPS wind speeds—available only every three hours—do not correspond with that of the boundary forcing, and further may contain phase errors. Thus, a third independent estimate of wind vector was derived based on observed high-frequency wave energy. An automated procedure works as follows:

- A sequence of SWAN simulations were performed, each with a different 10 m wind speed, ranging from 4 to 25 m/s, at 1 m/s increments. The grid design was similar to that used in the actual hindcasts, but there was no boundary forcing and the wind direction was always from 318° (directed offshore). These simulations were used to create a database on variation of one-dimensional spectra with wind speed.
- For each waverider spectrum, the high-frequency tail is identified.
- The energy level in this frequency range (specifically, the frequency-integrated variance) is compared with a similar integration of the database spectra and the most closely matching wind speed is selected for use in the actual hindcast.
- The wind direction is assumed to be identical to the mean direction of the high-frequency tail.

The measured spectra were often of complex mixed sea/swell conditions, so the most significant challenge with this automated procedure was to correctly identify the windsea portion of each spectrum without a priori knowledge of the wind speed. A quality-control procedure was developed to flag dubious solutions and exclude these cases from the set of hindcasts.

The inferred winds are specific to a single point, the waverider buoy location. In the wave model applications, this is applied uniformly over the domain, so the reduction of wind speeds by frictional effects over land is not accounted for in the wave model.

The three independent estimates of wind speed are shown in Fig. A1; here the NOGAPS time series is for the sea point (52°W, 33°S). The mean wind speed of the inferred and NOGAPS estimates is roughly similar, and the anemometer estimates are much smaller than both. The inferred and NOGAPS wind speeds are expected to be more representative of the winds that would generate waves arriving at the nearshore gages. Selection of one of the two is subjective, since each contained unknown errors. NOGAPS, since it is a global model, uses relatively coarse native geographic resolution, which is potentially a problem, especially near coastlines. The inferred wind speeds also contain errors, being sensitive to errors in the wave generation physics of the wave model. However, since these errors in wave generation physics would be replicated in the actual hindcasts, it can be argued that—in the hindcast application—the inferred wind speeds are more likely to produce windsea growth similar to that which is observed, even though the wind speeds themselves are not necessarily more accurate than those of NOGAPS. Further, the temporal structure of the inferred wind speeds corresponds directly with that of the boundary forcing, in contrast to NOGAPS. Thus, the inferred wind speeds are selected for the hindcasts.

As was mentioned in Section 4, 97 of 528 time periods were discarded due to mismatch of wave height at the offshore boundary, indicative of problems with wave growth internally. This was a surprising result, since the wind speed inference
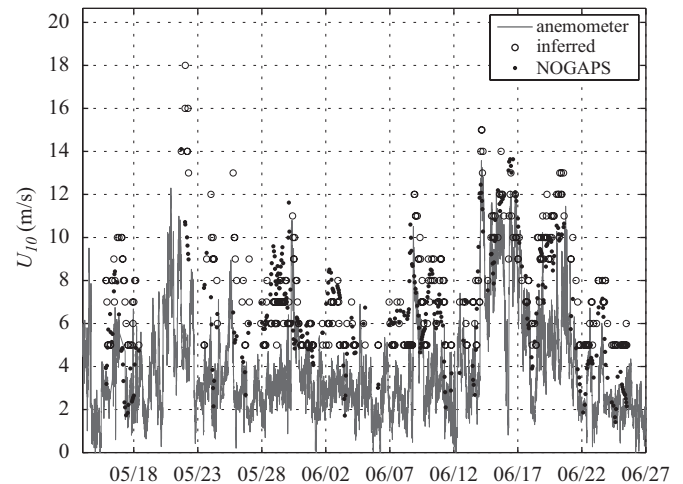

Fig. A1. Time series of wind speed by three independent estimates.

algorithm should provide the optimal wind speed for producing in the model the same wind sea as observed at the buoy. The discrepancy was found to be due to non-physical dependence of the whitecapping term on mean steepness: a problem that is improved—but apparently not eliminated—using the van der Westhuysen et al. (2007) source terms. Specifically, windsea component propagating nearly parallel with the offshore boundary was found to grow too quickly when swell is present. Since the wind speed inference algorithm is applied without swell present, inferred wind speeds are not affected by this problem, while the actual simulations are. In any event, the decision to omit these simulations was somewhat subjective, since it was not actually determined whether this spurious windsea component significantly affects nearshore comparisons.

References

Booij, N., Ris, R.C., Holthuijsen, L.H., 1999. A third-generation wave model for coastal regions, Part 1: Model description and validation. Journal of Geophysical Research 104 (C4), 7649–7666.

Cardone, V.J., Graber, H.C., Jensen, R.E., Hasselmann, S., Caruso, M.J., 1995. In search of the true surface wind field in SWADE IOP-1: Ocean wave modeling perspective. The Global Atmosphere and Ocean System 3, 107–150.

Dalrymple, R.A., Liu, P.L.-F., 1978. Waves over soft muds: a 2-layer fluid model. Journal of Physical Oceanography 8, 1121–1131.

Dean, R.G., Dalrymple, R.A., 1991. Water Wave Mechanics for Engineers and Scientists. World Scientific Publishing, p. 353.

De Wit, P.J., 1995. Liquefaction of cohesive sediment by waves. Ph.D. dissertation. Delft University of Technology, the Netherlands.

Dingemans, M.W., 1998. A review of the physical formulations in SWAN. WL|Delft Hydraulics Report H3306, Delft, the Netherlands, p. 69.

Gade, H.G., 1958. Effects of a non-rigid, impermeable bottom on plane surface waves in shallow water. Journal of Marine Research 156 (2), 61–82.

Hasselmann, K., Coauthors, 1973. Measurements of wind wave growth and swell decay during the Joint North Sea Wave Project (JONSWAP). Herausgegeben vom Deutsch. Hydrograph. Institut, Reihe A, 12, p. 95.

Hogan, T.F., Rosmond, T.E., 1991. The description of the US Navy operational global atmospheric prediction system's spectral forecast models. Monthly Weather Review 119, 1786–1815.

Holthuijsen, L.H., Booij, N., Ris, R.C., 1993. A spectral wave model for the coastal zone, In: Proceedings of the Second Symposium on Ocean Wave Measurements and Analysis, New Orleans, pp. 630–641.

Holthuijsen, L.H., Booij, N., Ris, R.C., and coauthors, 2006. SWAN Cycle III version 40.51 User Manual, p. 111 ⟨http://fluidmechanics.tudelft.nl/swan/index.htm⟩.

Hsiao, S.V., Shemdin, O.H., 1980. Interaction of ocean waves with a soft bottom. Journal of Physical Oceanography 10, 605–610.

Jiang, L., Mehta, A.J., 1995. Mudbanks of the southwest coast of India. IV: mud viscoelastic properties. Journal of Coastal Research 11 (3), 918–926.

Jiang, L., Mehta, A.J., 1996. Mudbanks of the southwest coast of India. V: wave attenuation. Journal of Coastal Research 12 (4), 890–897.

Kaihatu, J.M., Sheremet, A., Holland, K.T., 2007. A model for the propagation of nonlinear surface waves over viscous muds. Coastal Engineering 54 (10), 752–764.

Komen, G.J., Cavaleri, L., Donelan, M., Hasselmann, K., Hasselmann, S., Janssen, P.A.E.M., 1994. Dynamics and Modelling of Ocean Waves. Cambridge University Press, p. 532.

Lygre, A., Krogstad, H.E., 1986. Maximum entropy estimation of the directional distribution in ocean wave spectra. Journal of Physical Oceanography 16, 2052–2060.

MacPherson, H., 1980. The attenuation of water waves over a non-rigid bed. Journal of Fluid Mechanics 97 (4), 721–742.

Madsen, O.S., Poon, Y.–K., Graber, H.C., 1988. Spectral wave attenuation by bottom friction: Theory. In: The Proceedings of the 21st International Conference on Coastal Engineering. ASCE, NewYork, pp. 492–504.

Mei, C.C., Liu, K.-F., 1987. A Bingham-plastic model for a muddy seabed under long waves. Journal of Geophysical Research 92, 14581–14594.

Ng, C.O., 2000. Water waves over a muddy bed: a two-layer Stokes' boundary layer model. Coastal Engineering 40 (3), 221–242.

Plant, N.G., Holland, K.T., Puleo, J.A., 2002. Analysis of the scale of errors in nearshore bathymetric data. Marine Geology 191 (1-2), 71–86.

Ris, R. C., 1997. Spectral modeling of wind waves in coastal areas. Ph.D. Thesis, Delft University of Technology, p. 160.

Rogers, W.E., Hwang, P.A., Wang, D.W., 2003. Investigation of wave growth and decay in the SWAN model: Three regional-scale applications. Journal of Physical Oceanography 33, 366–389.

van der Westhuysen, A.J., Zijlema, M., Battjes, J.A., 2007. Nonlinear saturation-based whitecapping dissipation in SWAN for deep and shallow water. Coastal Engineering 54 (2), 151–170.

Vinzon, S.B., Winterwerp, J.C, Nogueira, R., Mud deposit formation on the open coast of the larger Patos Lagoon–Cassino Beach system. Continental Shelf Research, this volume, doi:10.1016/j.csr.2008.09.021.

WAMDI Group, 1988. The WAM model—A third generation ocean wave prediction model. Journal of Physical Oceanography 18, 1775–1810.

Winterwerp, J.C., de Graaff, R.F., Groeneweg, J., Luyendijk, A.P., 2007. Modelling of wave damping at Guyana mud coast. Coastal Engineering 54, 249–261.

Yan, L., 1987. An improved wind input source term for third generation ocean wave modelling, Scientific report WR-No 87-8, De Bilt, The Netherlands.

Zhang, X.-Y., Ng, C.-O., 2006. Mud-wave interaction: a viscoelastic model. China Ocean Engineering 20 (1), 15–26.

Zijlema, M., van der Westhuysen, A.J., 2005. On convergence behaviour and numerical accuracy in stationary SWAN simulations of nearshore wind wave spectra. Coastal Engineering 52 (3), 237–256.